Class. Quantum Grav. **25** (2008) 225001 (20pp) doi:10.1088/0264-9381/25/22/225001

Search for gravitational waves associated with GRB 050915a using the Virgo detector

F Acernese[ac,1], M Alshourbagy[ab,2], P Amico[ab,3], F Antonucci[a,4], S Aoudia[5], K G Arun[6], P Astone[a,4], S Avino[ab,1], L Baggio[7], G Ballardin[8], F Barone[ac,1], L Barsotti[ab,2], M Barsuglia[6], Th S Bauer[a,9], S Bigotta[ab,2], S Birindelli[ab,2], M A Bizouard[6], C Boccara[10], F Bondu[5], L Bosi[a,3], S Braccini[a,2], C Bradaschia[a,2], A Brillet[5], V Brisson[6], D Buskulic[7], G Cagnoli[a,11], E Calloni[ab,1], E Campagna[ac,11], F Carbognani[8], F Cavalier[6], R Cavalieri[8], G Cella[a,2], E Cesarini[ab,11], E Chassande-Mottin[5], S Chatterji[a,4], N Christensen[8], F Cleva[5], E Coccia[ab,12], C Corda[ab,2], A Corsi[a,4,14], F Cottone[ab,3], J-P Coulon[5], E Cuoco[8], S D'Antonio[a,12], A Dari[ab,3], V Dattilo[8], M Davier[6], R De Rosa[ab,1], M Del Prete[ac,2], L Di Fiore[a,1], A Di Lieto[ab,2], M Di Paolo Emilio[ac,12], A Di Virgilio[a,2], M Evans[8], V Fafone[ab,12], I Ferrante[ab,2], F Fidecaro[ab,2], I Fiori[8], R Flaminio[13], J-D Fournier[5], S Frasca[ab,4], F Frasconi[a,2], L Gammaitoni[ab,3], F Garufi[ab,1], E Genin[8], A Gennai[a,2], A Giazotto[a,2,8], L Giordano[ab,1], V Granata[7], C Greverie[5], D Grosjean[7], G Guidi[ac,11], S Hamdani[8], S Hebri[8], H Heitmann[5], P Hello[6], D Huet[8], P La Penna[8], M Laval[5], N Leroy[6], N Letendre[7], B Lopez[8], M Lorenzini[ab,11], V Loriette[10], G Losurdo[a,11], J-M Mackowski[13], E Majorana[a,4], N Man[5], M Mantovani[8], F Marchesoni[ab,3], F Marion[7], J Marque[8], F Martelli[ac,11], A Masserot[7], F Menzinger[8], L Milano[ab,1], Y Minenkov[a,12], C Moins[8], J Moreau[10], N Morgado[13], S Mosca[ab,1], B Mours[7], I Neri[ab,3], F Nocera[8], G Pagliaroli[a,12], C Palomba[a,4], F Paoletti [a,2,8], S Pardi[ab,1], A Pasqualetti[8], R Passaquieti[ab,2], D Passuello[a,2], F Piergiovanni[ac,11], L Pinard[13], R Poggiani[ab,2], M Punturo[a,3], P Puppo[a,4], O Rabaste[5], P Rapagnani[ab,4], T Regimbau[5], A Remillieux[13], F Ricci[ab,4], I Ricciardi[ab,1], A Rocchi[a,12], L Rolland[7], R Romano[ac,1], P Ruggi[8], G Russo[ab,1], D Sentenac[8], S Solimeno[ab,1], B L Swinkels[8], R Terenzi[a,12], A Toncelli[ab,2], M Tonelli[ab,2], E Tournefier[7], F Travasso[ab,3], G Vajente[ad,2], J F J van den Brand[ab,9], S van der Putten[a,9], D Verkindt[7], F Vetrano[ac,11], A Viceré[ac,11], J-Y Vinet[5], H Vocca[a,3] and M Yvert[7]

[1] INFN, Sezione di Napoli [a]; Università di Napoli 'Federico II'[b] Complesso Universitario di Monte S. Angelo, I-80126 Napoli; Università di Salerno, Fisciano, I-84084 Salerno[c], Italy
[2] INFN, Sezione di Pisa[a]; Università di Pisa[b]; Scuola Normale Superiore[c], I-56127 Pisa; Università di Siena, I-53100 Siena[d], Italy
[3] INFN, Sezione di Perugia[a]; Università di Perugia[b], I-6123 Perugia, Italy
[4] INFN, Sezione di Roma[a]; Università 'La Sapienza'[b], I-00185 Roma, Italy
[5] Departement Artemis, Observatoire de la Côte d'Azur, CNRS, F-06304 Nice, France
[6] LAL, Université Paris-Sud, IN2P3/CNRS, F-91898 Orsay, France

[14] Permanent address: Istituto di Astrofisica Spaziale e Fisica Cosmica, IASF-Roma/INAF, Via Fosso del Cavaliere, 100-00133 Roma, Italy.

[7] Laboratoire d'Annecy-le-Vieux de Physique des Particules (LAPP), IN2P3/CNRS, Université de Savoie, F-74941 Annecy-le-Vieux, France
[8] European Gravitational Observatory (EGO), I-56021 Cascina (Pi), Italy
[9] National institute for subatomic physics, NL-1009 DB[a]; Vrije Universiteit, NL-1081 HV[b], Amsterdam, The Netherlands
[10] ESPCI, CNRS, F-75005 Paris, France
[11] INFN, Sezione di Firenze, I-50019 Sesto Fiorentino[a]; Università degli Studi di Firenze, I-50121[b], Firenze; Università degli Studi di Urbino 'Carlo Bo', I-61029 Urbino[c], Italy
[12] INFN, Sezione di Roma Tor Vergata[a]; Università di Roma Tor Vergata[b], I-00133 Roma; Università dell'Aquila, I-67100 L'Aquila[c], Italy
[13] Laboratoire des Matériaux Avancés (LMA), IN2P3/CNRS, F-69622 Villeurbanne, Lyon, France

E-mail: Alessandra.Corsi@iasf-roma.inaf.it

Received 25 March 2008, in final form 16 June 2008
Published 23 October 2008
Online at stacks.iop.org/CQG/25/225001

Abstract
In the framework of the expected association between gamma-ray bursts and gravitational waves, we present results of an analysis aimed to search for a burst of gravitational waves in coincidence with gamma-ray burst 050915a. This was a long duration gamma-ray burst detected by *Swift* during September 2005, when the Virgo gravitational wave detector was engaged in a commissioning run during which the best sensitivity attained in 2005 was exhibited. This offered the opportunity for Virgo's first search for a gravitational wave signal in coincidence with a gamma-ray burst. The result of our study is a set of strain amplitude upper limits, based on the loudest event approach, for different but quite general types of burst signal waveforms. The best upper limit strain amplitudes we obtain are $h_{rss} = \mathcal{O}(10^{-20})$ Hz$^{-1/2}$ around ~200–1500 Hz. These upper limits allow us to evaluate the level up to which Virgo, when reaching nominal sensitivity, will be able to constrain the gravitational wave output associated with a long burst. Moreover, the analysis presented here plays the role of a prototype, crucial in defining a methodology for gamma-ray burst triggered searches with Virgo and opening the way for future joint analyses with LIGO.

PACS numbers: 95.55.Ym, 95.85.Sz, 97.60.−s, 98.70.Rz

(Some figures in this article are in colour only in the electronic version)

1. Introduction

Gamma-ray bursts (GRBs) are intense flashes of γ-ray (and x-ray) photons, lasting from few milliseconds to several minutes, followed by a fainter and fading emission at longer wavelengths called the 'afterglow' [1, 2]. GRBs are detected at a rate of about one per day, from random directions in the sky. They fall into two apparently distinct categories, namely short-duration (nominally, less than 2 s), hard-spectrum bursts (short GRBs) and long-duration (greater than 2 s), soft-spectrum bursts (long GRBs) [3–6]. Of course, this separation is not strict and the two populations do overlap, but such a distinction has suggested two different types of progenitors. Progenitors of long GRBs are thought to be massive, low-metallicity stars exploding during collapse of their cores; mergers of neutron stars (NSs) probably represent the most popular progenitor model of short GRBs at the present time [1, 2].

GRBs are likely to be associated with a catastrophic energy release in stellar mass objects. The sudden emission of a large amount of energy in a compact volume (of the order of tens of kilometers cubed), leads to the formation of a relativistic 'fireball' of $e^{\pm}$ pairs, γ-rays and baryons expanding in the form of a jet, while part of the gravitational energy liberated in the event is also converted into gravitational waves (GWs) [1, 2]. In the standard fireball model, the GRB electromagnetic emission is thought to be the result of kinetic energy dissipation within the relativistic flow, taking place at distances greater than $\sim 10^{13}$ cm from the source [1, 2]. The electromagnetic signal can give indirect but important information on the progenitor's nature (e.g. its properties can constrain the structure and density of the circumburst medium and it allows the identification of host galaxies). However, to reach a clearer understanding of the phenomenon, one should search for a direct signature of the progenitor's identity, which may be observed through the gravitational window. The energy that is expected to be radiated in GWs during the catastrophic event leading to a GRB would, in fact, be produced in the immediate neighborhood of the source. Thus, the observed GW signal would carry direct information on the properties of the progenitor.

In this paper, we present an analysis of the Virgo data [7] simultaneous with the long GRB 050915a [8], with the goal to constrain the amplitude of a possible short burst of GWs associated with this GRB. At the time of GRB 050915a, Virgo was engaged in a five-day long data run, named C7. Virgo's sensitivity during C7 exceeded that of all its previous runs. The lowest strain noise was $\sim 6 \times 10^{-22}$ Hz$^{-1/2}$ around $\sim$300 Hz. This is the first time a study of this kind has been performed on Virgo data, so the work presented here also aims to define a procedure of analysis for GRB searches with Virgo. In the very near future, these kinds of studies will take advantage of the joint collaboration with LIGO, and the existence of an established procedure is fundamental.

The sensitivity of Virgo during C7 was comparable to that of LIGO at the time when a coincidence search with GRB 030329 was performed [9], and the upper limits that we set for GRB 050915a are of the same order of magnitude, i.e. $\mathcal{O}(10^{-20}\ \mathrm{Hz}^{-1/2})$. The LIGO results on GRB 030329 thus represent a natural comparison for our analysis, even if procedures followed in this study were developed for a single-detector search, while those of the LIGO study were for a double-detector search.

In what follows, we first present an overview of the Virgo detector and its status during C7 (section 2). Then, we recall the scenarios for GRB progenitors and their associated GW emission (section 3), and we describe the main properties of GRB 050915a (section 4). Furthermore, we present the analysis of Virgo data in coincidence with GRB 050915a (section 5) and finally discuss our results (section 6).

2. The Virgo detector

The Virgo gravitational wave detector, jointly funded by INFN (Italy) and CNRS (France), is located near Pisa, at the European Gravitational Observatory (EGO). It is a power recycled Michelson interferometer with $l = 3$ km long arms, each containing a Fabry–Perot cavity (see, e.g., [10] for a recent review of Virgo's status).

GW interferometric detectors [11] have different types of source targets for their searches. These can be usefully divided into four main classes: stochastic waves, bursts, coalescing binaries and periodic waves. Sources that contribute to the first class are e.g. binary stars and primordial GWs (e.g. [12–14]). GW signals of the other three classes are produced e.g.

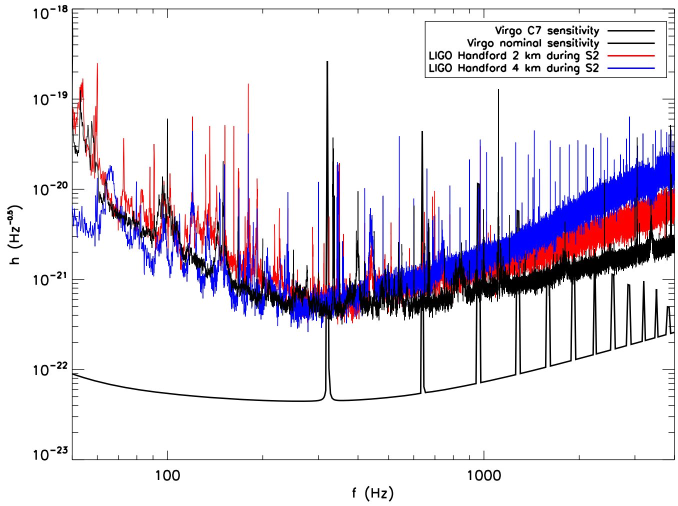

Figure 1. The Virgo sensitivity during the C7 run and the Virgo nominal sensitivity are plotted in black. Typical LIGO Hanford sensitivities during the S2 are shown in red (2 km) and blue (4 km) [39].

(This figure is in colour only in the electronic version)

by compact binaries and their coalescence (e.g. [15] and references therein), rotating NSs with a non axis-symmetric mass distribution along the rotation axis or NSs instabilities (e.g. [16–18]), collapse of massive stars and supernova (SN) explosions (e.g. [19] and references therein). GRBs, short and long, are thought to be linked respectively to the coalescence of compact binaries and collapse of massive stars [2], and this has motivated searches for GWs signals in association with these sources [9, 20–36].

By the beginning of September 2005, Virgo was engaged in a commissioning run named C7, with the aim to test the gain in sensitivity after several improvements were performed on the detector (see [37] for a review of Virgo status during C7). The run lasted five days, with a duty cycle of ∼65%, and a mean sensitivity such that an optimally oriented 1.4–1.4 $M_\odot$ NS–NS binary coalescence, at a distance of ∼1 Mpc, would have been detected with a signal-to-noise ratio of 8. Figure 1 shows a comparison of the Virgo sensitivity curve during C7, and the LIGO sensitivity during its second science run (S2), when a search for a burst of GWs in coincidence with GRB 030329 was performed [9].

The main physical information for the detection of GWs is extracted by reconstructing the interferometer strain. This fundamental step consists of the extraction of the arms' length relative difference $\delta l/l$, i.e. the amplitude of the GW signal, from the output dark fringe signal [38]. During the C7 run, the error in the h-reconstructed data ($h(t) = \delta l/l$) was estimated to be around ∼ +20%–40%. Hereafter, this is assumed as a systematic error in our analysis.

3. GRB progenitor models and the expected GW signal

The actual favored scenario for long GRB progenitors is the so-called collapsar model, which invokes the collapse of a massive star down to a black hole (BH) with formation of an accretion disc, in a peculiar type of SN-like explosion (see, e.g., [40–42]). On the other hand, the favored scenario for short GRB progenitors is the compact binary (NS–NS or BH–NS) merger. To produce a GRB, both long or short, it is required that the progenitor stellar system ends as a rotating BH and a massive disc of matter around it, whose accretion powers the GRB ultra-relativistic fireball in the form of a jet, along the rotational axis of the system [1]. Due to the relativistic beaming effect, only observers located within the jet opening angle are able to observe the emission from the jet. In the standard assumption (see, e.g., [43]), the jets are uniform, with sharp cut-offs at the edges, and the line of sight cuts right across the jet axis, i.e. the Earth is near the center of the γ-ray beam.

GWs are expected to be emitted in association with both long and short GRBs [44, 45]. For short ones, a chirp signal should be emitted in GWs during the in-spiral, followed by a burst-type signal associated with the merger and subsequently a signal from the ring-down phase of the newly formed BH [45]. For long GRBs, the high rotation required to form the centrifugally supported disc that powers the GRB should produce GWs emission via bar or fragmentation instabilities that might develop in the collapsing core and/or in the disc [45]. Moreover, asymmetrically in-falling matter is expected to perturb the final BH geometry, leading to a ring-down phase [45]. While an axis-symmetric rotating collapse and core bounce would give no contribution to GW emission along the GRB axis, bar and fragmentation instabilities are all dominated by modes with spherical harmonic indices $l = m = 2$ [46], implying that GRB progenitors would emit more strongly along the GRB axis than in the equatorial plane (i.e. the orbital plane of the disc fragments or of the bar). The same holds for the ringing BH [46]. Thus, in the standard scenario having the Earth near the center of the γ-ray beam, the detector is located in the maximum of the emission pattern for GWs dominated by spherical harmonic indices $l = m = 2$.

A final important aspect is the expected delay between the electromagnetic trigger and the associated GW signal. Typically for long GRBs (relevant for our analysis), a GW signal is searched for within a window of 180 s around the GRB trigger. For a GW burst associated with the formation of the GRB central engine, the electromagnetic trigger should follow the GW one. The time delay between the two being dominated by the time necessary for the fireball to push through the stellar envelop of the progenitor, which can be of the order of 10–100 s [47]. A period of 120 s before the trigger time is selected to over-cover these predictions. Moreover, given that some models predict a GW signal contemporaneous with the GRB emission (see [48]), the 60 s after the electromagnetic trigger are also included in our search.

4. GRB 050915a

On the 15th of September 2005, at T = 11 : 22 : 42 UT, the 'burst alert telescope' (BAT) on-board *Swift* [49] triggered and located GRB 050915a [8]. The BAT on-board calculated position was RA = 05h 26m 51s, Dec = −28 d 01′48″ (J2000), with an uncertainty of 3 arcmin. The BAT measured a T_{90} [15] duration of 53 ± 3 s in the 15–350 keV energy band [50], thus GRB 050915a was classified as a long-type GRB. The 'x-ray telescope' (XRT) began observing the BAT position at 11 : 24 : 09 UT (∼87 s after the trigger [51]). The new refined position was RA = 05h 26 m 44.6 s, DEC = −28 d 01m 01.0 s [51]. Finally, the *Swift* 'ultra-violet and optical telescope' (UVOT) began observing the field of GRB 050915a ∼85 s after the BAT trigger [52], and the optical and IR follow-up of this burst was performed by different telescopes [53–58]. In the radio band, observations by the 'Very Large Array' (VLA) on September 18.58 UT revealed no radio source in the error circle [59]. Recently,

[15] The T_{90} duration is defined as the time necessary to collect from 5% to 95% of the total counts in the specified energy band.

evidence has been found for a possible distant and/or faint host galaxy [60, 61], however the redshift of this burst still remains unknown.

5. Coincidence analysis for a burst of GWs

Given the lack of accurate predictions on the expected GW waveforms that might be associated with long GRB progenitors, we have chosen in this search to look for a GW burst-type signal associated with GRB 050915a in a model independent way. Our analysis aims to:

- set-up a procedure for GRB triggered searches with Virgo, that goes well beyond the single case of GRB 050915a, but has a much more general interest, both in the context of GWs triggered searches and GRB research, and also in view of the future joint collaboration with LIGO;
- constrain the amplitude of the associated GW emission to quantify Virgo's capability to provide information pertaining to models for GW production by GRBs, and also to define possible margins of improvement in view of the expected enhancement in sensitivity;
- define an algorithm that will find application also for the categories of short GRBs (merger and ring-down phase, see section 3), which are expected to be nearer and thus more promising sources of GWs than long bursts.

5.1. Wavelet analysis

For our analysis, we relied on a new wavelet-based transient detection tool, the wavelet detection filter (WDF). Wavelets were introduced in the 1980s as a mathematical tool to represent data in both time and frequency [62]. The wavelet transform is defined as the correlation of the data $x(t)$ against the wavelets $\psi_{a,b}$,

$$W_x(a,b) = \int_{-\infty}^{+\infty} x(t)\psi_{a,b}(t)\,\mathrm{d}t. \tag{1}$$

The wavelet family is obtained by translations and dilations of a reference waveform ψ:

$$\psi_{a,b}(t) = \frac{1}{\sqrt{a}}\psi\left(\frac{t-b}{a}\right). \tag{2}$$

The wavelet transform gives a representation of the signal in terms of the scale a (associated with frequency) and time b. The reference wavelet $\psi(t')$ is chosen to be a zero-mean function of unit energy, well localized both in time (around $t' = 0$) and frequency. Consequently, this is a short-duration waveform with few cycles. Wavelet-based representations are well suited for burst-like signals because of similarities between those signals and the analyzing wavelet ψ.

The wavelet family is redundant but when the sampling of the scale a and time b axes is dyadic i.e., when $(a_j, b_k) = (2^j, k2^j)$ for $j \geqslant 0$ and k integers, it forms an orthonormal basis, provided some geometrical constraints on the choice of ψ are set (we will not detail them here, the reader is referred to [62]). The wavelet transform produced in this way is referred to as a *discrete wavelet transform*, and we use it to analyze the data. Since we are dealing with signals sampled at a rate of $f_s = 20$ kHz, and we consider data blocks of N samples, the dyadic sampling is limited to the range $j = 0, \ldots, \log_2 N$ and $b_k/a_j = k/f_s$ with $k = 0, \ldots, N-1$.

5.2. Best matching wavelets and thresholding

The wavelet transform can be viewed as a bank of matched filters. We select the best matching wavelets (largest correlation coefficients) by thresholding. Let us define the soft-thresholding operator $T(w;\eta) = sign(w)(|w| - \eta)$ if $|w| > \eta$ and 0 otherwise, and the thresholded coefficients of the discrete wavelet transform $w_{j,k} = T(W_x(a_j, b_k); \eta)$.

We use the signal-to-noise ratio (S_w) as a statistic

$$S_w = \sqrt{\frac{\sum_{j,k} w_{j,k}^2}{\sigma_n^2}} \tag{3}$$

to discriminate the presence or absence of a burst-like signal in the data, with σ_n^2 being an estimate of the variance of the noise. The threshold choice is $\eta = \sqrt{2\log N}\sigma_n$. This choice is linked to a general result by Donoho and Johnstone [63] concerning non-parametric denoising. Let our data $x(t) = s(t) + n(t)$ be the sum of a signal $s(t)$ and Gaussian white noise $n(t)$. It can be shown that the signal estimate obtained as

$$\hat{s}(t) = \sum_{j,k} w_{j,k}\psi_{a_j,b_k}(t), \tag{4}$$

i.e. by inverting the thresholded wavelet transform, minimizes the mean-square error over a broad class of signals [64].

5.3. Pipeline: preprocessing, analysis and trigger selection

We preprocess the data by applying a time-domain whitening procedure [66] using an estimate of the noise spectral density given by an autoregressive (AR) fit over the first 1000 s of the data set. We divide the whitened time-series into overlapping blocks of duration $\Delta t_W = 12.8$ ms, which also sets the time resolution of the search. The epochs of two successive blocks differ by $\Delta t_s = 0.6$ ms.

We already mentioned that the wavelet basis may be interpreted as a template grid. It is well known that redundant grids are better suited for burst detection because they increase the chance of a good match between the signal and one of the templates. Instead, the wavelet bases are sparse by construction. To compensate for this sparsity, we insert redundancy by combining the results from several wavelet decompositions. We empirically select 18 different wavelets (including Daubechies wavelets from 4 to 20 [62], the Haar wavelet and the windowed Discrete Cosine [64]). For each data block, we compute these 18 wavelet transforms. Thus, we obtain 18 S_w estimates and select the largest one (*SNR*). Furthermore, we generate a shorter trigger list by selecting only *SNR* values larger than 4.

Typically, the energy content of a burst signal will be tracked by the WDF in the form of a 'cluster' of successive triggers, each containing a different fraction of its energy. To assign to each candidate event a unique time and *SNR* value, the clustering should be properly organized. As such, we cluster all triggers with a time difference less than 10 ms ($\sim\Delta t_W$). For each cluster, a candidate event is defined by the time and *SNR* of the trigger at which the maximum *SNR* of the cluster is reached, i.e. where the signal leaves most of its energy.

5.4. The analysis method

For our analysis, we rely on a single stretch of data during which the interferometer was maintained in the same configuration and the *h*-reconstruction processes were recognized as good. Such a stretch is between the GPS times 810 808 602 s and 810 825 638 s, for a total of 16 836 s, containing the GRB trigger time (i.e. GPS time ∼810 818 575 s). We define as the on-source region a data segment 180 s long, 120 s before the GRB trigger time and 60 s after (see the thick-solid line in figure 2). This is the time window where we searched for a coincidence with the GRB trigger. The rest of the data in the stretch, with the exception 60 s

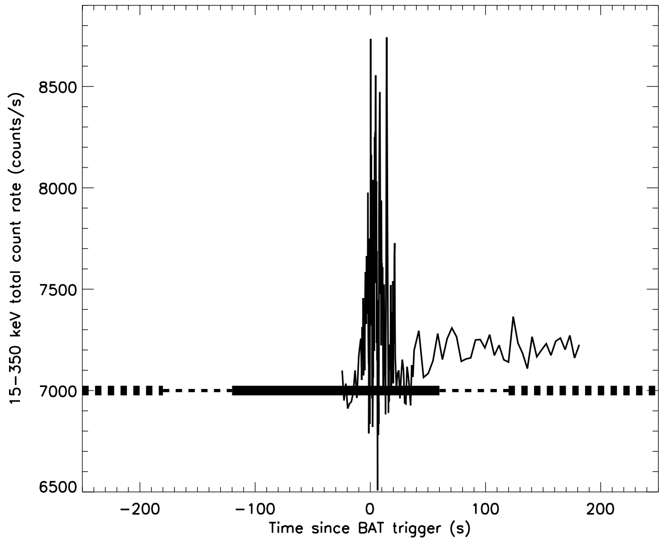

Figure 2. BAT (15–350 keV) light curve of GRB 050915a in total count rate (counts s^{-1}, thin solid line). Data of the BAT light curve for GRB 050915a have been downloaded from the online archive [65]. The thick solid line defines the time length and position of the on-source region, the thin-dashed segments mark the 60 s of data before the start and after the end of the signal region which are excluded from the analysis (so to separate the background from the signal); the thick-dashed segments mark the portions of the off-source region around the GRB trigger time. The whole off-source region considered in our analysis is much longer, extending on the left of the plot up to −9973 s and on the right of the plot up to 6863 s.

before the start and after the end of the signal region (see the thin-dashed in figure 2), belong to what we define as the off-source region (see the thick-dashed lines in figure 2). The analysis of the off-source region is used to assess the data quality and to study the statistical properties of the background. As explained in section 3, the on-source region has been chosen to start 120 s before the trigger time, so as to over-cover most of astrophysical predictions regarding the expected delay between the GRB and the associated burst-type GW signal. Moreover, in view of models that predict a GW signal contemporaneous with the GRB emission and considering that GRB 050915a had a T_{90} duration of 53 ± 3 s (see section 4), we have chosen our signal region to end 60 s after the trigger. The same choice for the time-length of the on-source region was also implemented in [9], for the case of the long GRB 030329.

Our pipeline is calibrated by adding simulated signals of various amplitudes and waveforms to data in the off-source region. The simulated signals were produced using the Virgo SIESTA simulation code [67]. The resulting data stream is processed in the same way as for the off- and on-source regions. Using simulated signals we evaluate the detection efficiency as a function of the simulated signal strength, which we quantify in terms of root-sum square amplitude of the incoherent sum of the contributions from the ‘plus’ and ‘cross’ polarizations:

$$h_{rss} = \sqrt{\int_{-\infty}^{+\infty} \left(h_+^2(t) + h_\times^2(t)\right) \mathrm{d}t}. \tag{5}$$

This allows us to make physical interpretations with the results.

The calibration procedure is based on simulations of plausible but quite general burst-type waveforms, with different amplitudes, characteristic frequencies and durations, chosen on the basis of the considerations explained in section 5.5. The times at which those signals are added to the off-source data are randomly determined by following a Poisson distribution with a mean rate of 0.1 Hz.

Knowledge of the source position is also used when adding the simulated signals to the off-source data, by considering the antenna response at the GRB position and time. A GW arriving at the interferometer from the GRB direction can be described as a superposition of two polarizations amplitudes h_+ and $h_\times$. The response of the interferometer to such a wave is given by [68]

$$\delta l/l = h(t) = F_+ h_+(t) + F_\times h_\times(t), \tag{6}$$

where F_+ and $F_\times$ are expressed as functions of the source position and of the polarization angle ψ [69], which describes the orientation of the wave frame in the detector frame. Note that for burst signals, since h_+ and $h_\times$ are in principle independent of each other, this orientation is fixed simply by convention (see, for example, [70]). However, if one assumes specific waveforms for h_+ and $h_\times$, such as both being sine-Gaussians, one may introduce a polarization angle parameter to conveniently control the relative power in the two polarizations. The antenna pattern functions F_+ and $F_\times$ can be written as

$$F_+ = F_+^0 \cos(2\psi) - F_\times^0 \sin(2\psi) \tag{7}$$

$$F_\times = F_+^0 \sin(2\psi) + F_\times^0 \cos(2\psi), \tag{8}$$

where $F_+(\psi = 0) = F_+^0$ and $F_\times(\psi = 0) = F_\times^0$. In the case of GRB 050915a, we have $F_+^0 \sim 0.32$ and $F_\times^0 \sim 0.21$.

5.5. *Choice of plausible waveforms*

5.5.1. Gaussian waveforms. To calibrate our pipeline, considering the great uncertainties in the waveforms associated with long GRB progenitors, we added different burst-type signals to the off-source data. Our simplest choice was for Gaussian signals, having the following form:

$$h(t) = h_0 \exp[-(t - t_0)^2/2\sigma^2] F_+^0 \tag{9}$$

where t_0 is the time at which the signal is added to the off-source data stream, and σ values of 0.5 ms, 1 ms and 1.5 ms were considered. These were broad-band, linearly polarized waveforms along the + direction, with the unknown polarization angle ψ set to zero. Note that for a given value of σ and h_0, a different choice of ψ rescales the waveform amplitude arriving at the detector by a factor of $\cos(2\psi)$, while leaving unchanged its shape over the detector bandwidth. Thus, the efficiency curves for the general ψ case can be estimated from the $\psi = 0$ ones presented here, by rescaling the h_{rss} corresponding to a given detection efficiency for a factor of $\frac{1}{\cos(2\psi)}$.

5.5.2. Sine-Gaussian waveforms. To mimic GW emission by GRB progenitors during the phase of collapse, fragmentation or bar instabilities, we considered sine-Gaussian waveforms. Taking a best case model scenario of GW emission from a triaxial ellipsoid rotating about the same axis as the GRB (i.e., the direction to the Earth, see equations (A.3) and (A.4) in appendix A), and using a Gaussian amplitude as the simplest way to mimic the impulsive character of a GW burst, we consider signals having in the wave frame the following form:

$$h_+ = h_0 \exp[-(t - t_0)^2/2\sigma^2] \cos(2\pi f_0 (t - t_0)) \tag{10}$$

$$h_\times = h_0 \exp[-(t-t_0)^2/2\sigma^2] \sin(2\pi f_0(t-t_0)) \tag{11}$$

for an unknown value of polarization angle ψ. The detector response to such types of signals is then computed using equations (7) and (8). After some algebra, the resulting $h(t)$ can be written as

$$h(t) = h_0 \exp[-(t-t_0)^2/2\sigma^2]\big[F_+^0 \cos(2\pi f_0(t-t_0) - 2\psi) + F_\times^0 \sin(2\pi f_0(t-t_0) - 2\psi)\big]. \tag{12}$$

In our analysis we set $\psi = 0$ and span the frequency range $f_0 \sim 200$–1500 Hz, as suggested by the predictions for GW emission from GRB progenitors, when fragmentation or bar instabilities are developed (see dash-dotted lines in figures 3–5 of [45]). For each f_0, we consider two values of Q, i.e. $Q = 5$ and $Q = 15$.

It is worth noting that for signals of the form (10)-(11) with $Q = 2\pi f_0 \sigma \gtrsim 3$ (i.e. for relatively narrow-band signals), one has

$$h_{rss} \simeq \sqrt{h_0^2 \frac{Q}{2\sqrt{\pi} f_0}} \tag{13}$$

and

$$\sqrt{\int_{-\infty}^{+\infty} h^2(t)\,\mathrm{d}t} \simeq h_{rss} \sqrt{\frac{\left(F_+^0\right)^2 + \left(F_x^0\right)^2}{2}} \tag{14}$$

where $h(t)$ is given by equation (12). In this approximation, if the detector noise is roughly constant within the relatively narrow signal bandwidth, the detected *SNR* is proportional to the above integral. Thus, the detection efficiency as a function of the h_{rss} is expected to be independent of the choice of ψ.

5.5.3. Damped sinusoid waveforms. Consider now the phase of BH ringing. A Kerr BH distortion can be decomposed into spheroidal modes with spherical-harmonic-like indices l and m (see, e.g., [71]). The quadrupole modes ($l = 2$) presumably dominate [71], while the paramount m-value depends upon the matter flow. In particular, the $m = \pm 2$ modes are bar-like, co-rotating ($m = +2$) and counter-rotating ($m = -2$) with the BH spin, and the $l = m = 2$ mode is expected to be the most slowly damped one. As underlined in [72], numerical simulations of a variety of dynamical processes involving BHs show that, at intermediate times, the response of a BH is indeed well described by a linear superposition of damped exponentials. Generally speaking, the polarization of the ring-down waveform will depend on the physical process generating the distortion of the BH (see, e.g., [73]). Since the $l = m = 2$ mode may be preferentially excited in the presence of binary masses or fragmentation of a massive disc, it is commonly assumed that the distribution of the strain between polarizations $h_+, h_\times$ for this mode mimics that of the in-spiral phase [46, 72, 74],

$$h_+ = h_0 \tfrac{1}{2}(1 + \cos^2\theta_0) \exp(-t/\tau) \cos(2\pi f_0 t + \xi)\Theta(t), \tag{15}$$

$$h_\times = h_0 \cos\theta_0 \exp(-t/\tau) \sin(2\pi f_0 t + \xi)\Theta(t), \tag{16}$$

where ξ is an arbitrary phase, θ_0 is the inclination of the angular momentum axis with respect to the source direction in the sky and $\Theta(t)$ is the normalized step function. Since we expect to observe the GRB on-axis, this polarization is also circular.

Thus, we added to the off-source region signals with the form

$$h(t) = h_0 \exp[-(t - t_0)/\tau] \times \left[F_+^0 \cos(2\pi f_0(t - t_0)) \Theta\left(1 - \frac{1}{4 f_0 (t - t_0)}\right) \Theta(t - t_0) + F_\times^0 \sin(2\pi f_0(t - t_0)) \Theta(t - t_0) \right], \tag{17}$$

where again $\Theta(t - t_0)$ and $\Theta\left(1 - \frac{1}{4 f_0 (t - t_0)}\right)$ are normalized step functions[16].

The characteristic frequency of the $l = m = 2$ quasi-normal mode of a Kerr BH is estimated as [45]

$$f_0 = 32\ \mathrm{kHz}\ (1 - 0.63(1 - a)^{3/10}) \left(\frac{M}{M_\odot}\right)^{-1}, \tag{18}$$

where a is the dimensionless spin parameter of the Kerr BH, while the damping time can be estimated as

$$\tau \sim (\Delta f)^{-1} = \pi f_0 / Q(a), \tag{19}$$

where $Q(a) = 2(1 - a)^{-9/20}$ [45, 75]. For GRB progenitors it is typically assumed $a = 0.98$, since the BH is supposed to have spun up to near maximal rotation by a massive accretion disc [45]. In the collapsar model, M is expected to be of the order of $\sim 1\ M_\odot$, which implies $f_0 \sim 10$ kHz [45], so a detection would be difficult.

However, the collapsar model for long GRBs is one of a larger class of proposed progenitor models, all leading to a final BH plus accretion disc system. Thus, the process of GW emission can always be described in a way similar to the collapsar case [45]: a high rotation rate producing bar or fragmentation instabilities in the disc, followed by a BH initially deformed encountering a ring-down phase. Among these variants of the collapsar model, the BH-white dwarf scenario may be characterized by higher BH masses ($M \sim 10\ M_\odot$) and lower f_0 values, down to ~ 1 kHz (see figure 3 of [45]). According to equation (19), a f_0 around 1 kHz would imply a damping time of ~ 0.3 ms. Thus, we choose to span a frequency range between ~ 800 Hz and 3 kHz, for τ values of 0.3 ms, 1 ms and 1.5 ms.

6. Results and discussion

6.1. Data quality

We applied the WDF to the data of the off-source region and derived the distribution of the trigger strengths. In the off-source region, we selected $\sim 2.1 \times 10^3$ triggers crossing the threshold $SNR = 4$. We processed the resulting list so as to eliminate triggers related to instrumental artifacts. The trigger rejection operates in two steps [76], namely a data preselection followed by a glitch removal procedure, that we can summarize as follows.

First, triggers falling into periods where known instrumental problems occurred (e.g. saturation of the control loop electronics, problems in the *h*-reconstruction process) or when aircraft (known to produce high seismic/acoustic noise which couples into the interferometer) fly over the instrument, are discarded. This preselection, while leaving the on-source region untouched, cuts out from the off-source segment (16 500 s) about 14 s associated with high acoustic noise, occurring about 1945 s after the start of the off-source stretch. Furthermore, a glitch removal procedure was applied. An extensive study has been performed to establish

[16] The reason for multiplying $\cos(2\pi f_0(t - t_0))$ by $\Theta(1 - \frac{1}{4 f_0 (t - t_0)})$ is to avoid a discontinuity at the beginning of the waveform, which would result in an infinite energy, even though h_{rss} would remain finite.

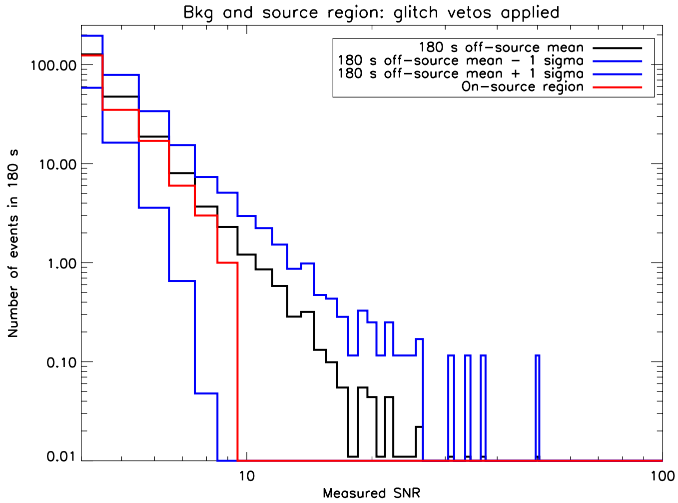

Figure 3. The mean *SNR* distribution found in the off-source region (black) and its $\pm 1\sigma$ interval (blue) is compared with the on-source *SNR* distribution (red). As is evident, the on-source distribution is within the 1σ interval around the mean off-source one, confirming that the on-source and off-source distributions are statistically compatible. Other basic checks were also applied, including a comparison of the off-source and on-source regions in the time–frequency domain, and a Kolmogorov–Smirnov test (90% confidence level, two-sided test) between the on- and off-source *SNR* distributions.

(This figure is in colour only in the electronic version)

the correlation of triggers produced by the burst search pipelines, and environmental or instrumental glitches occurring during C7 (see [76] for a detailed description). This study provided the definition of a series of veto criteria, based on information given by the auxiliary channels, and introduced a 'dead time' of ~6.3% [76] on the complete data set of the C7 run. The application of these criteria in our analysis leads to a dead time of ~582 s in the off-source region (i.e. ~3.5% of its duration) and of ~1.3 s in the on-source region (i.e. ~0.75% of its duration). The loudest on-source event remains unaffected by the veto procedure.

It is important to note that we have *not* applied *all* the vetoes designed for the C7 data. In fact, the majority of spurious burst triggers have been related to the so-called 'burst of burst' (BoB) [76]. BoBs originate from a misalignment of the interferometer mirrors, which increases the coupling of the laser frequency noise into the interferometer itself and causes a noise increase lasting up to a few seconds. Procedures have been defined to veto the BoBs. However, as estimated from the complete dataset of C7 run, these introduce a large dead time (~16% of the run duration [76]). Thus, since the BoB cuts can significantly affect the integrity of the on-source segment, we chose *not* to apply them. It is worth noting that during a BoB, the interferometer is sensitive to GWs, therefore we can still observe a possible GW counterpart of a GRB, albeit with a lower *SNR*.

6.2. Statistical analysis

We show in figure 3 the *SNR* distribution found in the off-source and on-source regions, where we have applied the data quality cuts described in section 6.1. The *SNR* distribution in the on-source region is confined below *SNR* = 9 (see figure 4). To test if the distribution of events observed on-source is compatible with being only noise, we performed different checks.

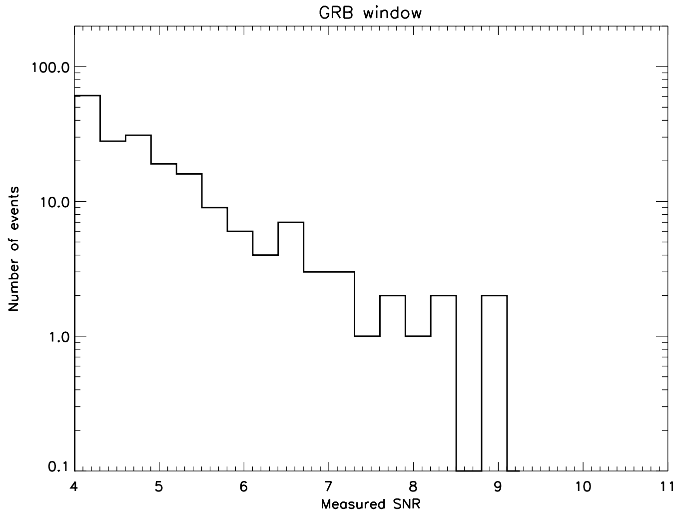

Figure 4. Distribution of event strengths in the on-source region (number of events versus detected *SNR*).

First, starting from the beginning of our data stretch (i.e. GPS 810808602 s), we sampled our background distribution by dividing the off-source region into ∼90 successive windows 180 s long. We find that the percentage of such windows having a loudest event with $SNR > 9$ is of about 89% (after applying in each of the windows the cuts described in the previous section). Second, we computed the mean *SNR* distribution on the 90 off-source windows and derived for each *SNR* bin the corresponding σ. As shown in figure 3, the on-source distribution is well within the $\pm 1\sigma$ interval around the mean off-source one, thus being compatible with noise. The same check was repeated with respect to the events duration, by constructing the mean distribution in the off-source windows, and comparing it with the on-source one. Also in this case, the on-source distribution turned out to be well within the $\pm 1\sigma$ interval around the mean off-source. As a result, in the *SNR* versus duration plane, the on-source events are distributed totally within the off-source ones.

From these tests we conclude that the on-source events are consistent with noise and that no clear evidence is found for an exceptional event, with respect to the background statistics, that could possibly be associated with the GRB. Thus, we move to the definition of an upper limit, by following the procedure described in [77]. To this end, we use simulated signals to determine the strain necessary to have 90% frequentist probability for such signals showing up as events with $SNR > 9$, i.e. with a *SNR* above that of the loudest event observed in the on-source region. This means estimating the efficiency ϵ at which the instrument and filtering process can detect burst events with $SNR > 9$. According to [77], the simulated signals are added to the *off-source data*, so as to evaluate ϵ with good statistics, thanks to the long duration of the chosen off-source stream. Before proceeding with the efficiency estimates, basic sanity checks aimed to guarantee the consistency of our approach were applied. These included a comparison of the off-source and on-source regions in the time-frequency domain, and a Kolmogorov-Smirnov test (90% confidence level, two-sided test) between the on- and off-source *SNR* distributions. The reader is referred to [36] for other sample tests which have been developed in the context of LIGO data analyses in coincidence with GRB triggers.

Table 1. h_{rss} upper limits for damped sinusoid, sine-Gaussian and Gaussian waveforms. The first two columns give details on the waveform parameter state, the third column is the h_{rss} for which 90% efficiency is reached in detecting simulated signals at *SNR* > 9. The error-bars account for the errors on the parameters of the best-fit efficiency curve. Note that these h_{rss} values are also affected by a systematic error, as described in sections 2 and 6.3.

Damped sinusoid			Sine-Gaussian			Gaussian	
τ (ms)	f_0 (Hz)	90% $h_{rss}^{DS} \times 10^{20}$ ($\mathrm{Hz}^{-1/2}$)	Q	f_0 (Hz)	90% $h_{rss}^{SG} \times 10^{20}$ ($\mathrm{Hz}^{-1/2}$)	σ (ms)	90%$h_{rss}^{G} \times 10^{20}$ ($\mathrm{Hz}^{-1/2}$)
0.3	807	$3.83^{+0.03}_{-0.02}$	5	203	2.42 ± 0.04	0.5	$2.74^{+0.02}_{-0.04}$
0.3	998	4.09 ± 0.06	5	497	$2.09^{+0.02}_{-0.04}$	1	$4.68^{+0.07}_{-0.08}$
0.3	1502	5.03 ± 0.08	5	803	$2.59^{+0.02}_{-0.01}$	2	$18.9^{+0.2}_{-0.1}$
0.3	1997	5.48 ± 0.07	5	1001	2.96 ± 0.03	–	–
0.3	3003	8.0 ± 0.1	5	1503	$3.78^{+0.08}_{-0.07}$	–	–
1	807	3.29 ± 0.03	15	203	$3.34^{+0.06}_{-0.07}$	–	–
1	998	$3.39^{+0.05}_{-0.06}$	15	497	$2.33^{+0.02}_{-0.03}$	–	–
1	1502	$4.16^{+0.05}_{-0.06}$	15	803	$2.79^{+0.05}_{-0.04}$	–	–
1	1997	$5.06^{+0.07}_{-0.08}$	15	1001	2.68 ± 0.03	–	–
1	3003	7.7 ± 0.1	15	1503	$3.04^{+0.01}_{-0.02}$	–	–
1.5	807	3.12 ± 0.04	–	–	–	–	–
1.5	998	$3.32^{+0.06}_{-0.07}$	–	–	–	–	–
1.5	1502	$3.81^{+0.04}_{-0.03}$	–	–	–	–	–
1.5	1997	$5.05^{+0.08}_{-0.07}$	–	–	–	–	–
1.5	3003	$7.48^{+0.10}_{-0.09}$	–	–	–	–	–

6.3. Detection efficiency and upper limit strain

The efficiency ϵ in detecting signals with $SNR > 9$ is estimated by computing for each kind of chosen waveform (see section 5.5), the percentage of simulated signals found by the pipeline, as a function of the injected strain amplitude h_{rss}. A simulated signal added to the noise at a given time t_0 is recognized by the pipeline at t_{det} if $|t_{\mathrm{det}} - t_0| \leqslant 20$ ms. This ± 20 ms coincidence window takes into account the duration of the wavelet decomposition window (12.8 ms), allowing a partial overlap. Moreover, a coincidence window of ± 20 ms contains the $\sim\pm 2\sigma$ portion of the longest duration simulated signal (sine-Gaussian waveforms with $Q = 15$ and frequency 203 Hz, having $\sigma \sim 12$ ms).

In table 1 we report the results obtained for different waveforms. The reported errors correspond to the $\pm 2\sigma$ uncertainty on the best fit curve. We also stress that the derived upper limits are affected by a +20%–40% systematic error, related to the uncertainties in the calibration of h-reconstruction (see also section 2). The lowest h_{rss} upper limit is obtained for the sine-Gaussian waveform at frequency $f_0 = 497$ Hz with $Q = 5$ for which $h_{rss}^{SG} \sim 2.09 \times 10^{-20}\ \mathrm{Hz}^{-1/2}$.

Considering sine-Gaussian waveforms, as one can see, the detection efficiency depends on the signal frequency. There are two main elements determining such dependence: (i) the detector noise level and (ii) the signal duration with respect to the window in which the wavelet decomposition is performed. Concerning point (i) consider two sine-Gaussian signals at different frequencies, with equal strain amplitude h_{rss}. Those will be detected at different *SNR* values, since the detector noise level changes with frequency. Thus the lowest the detector noise around the signal characteristic frequency the highest its detection efficiency. Concerning point (ii) sine-Gaussian waveforms with the same Q but differing f_0

have different durations (i.e. $5\sigma = 5\frac{Q}{2\pi f_0}$). The de-noising procedure we apply to estimate the event *SNR* (see section 5.2) is more efficient when the duration of the window in which the wavelet decomposition is performed is comparable to the signal duration. When taking a shorter wavelet window, part of the signal power is lost. On the other hand, choosing a wavelet window much longer than the signal duration implies that the probability for the background to survive the thresholding is enhanced, resulting in a loss of efficiency. This is the reason why in our analysis, as a trade-off, we set a wavelet decomposition window of 12.8 ms, comparable to the $\sigma \sim 12$ ms of the longest injected event.

For damped-sinusoid waveforms with τ values of 0.3 ms, 1 ms and 1.5 ms, given the h_{rss} and f_0 values, the detection efficiency decreases with decreasing τ (see table 1). On the other hand, for a given τ but different characteristic frequencies, the detection efficiency decreases with increasing f_0.

Finally, the simplest type of simulated waveforms is Gaussian ones. The 5σ durations of these signals are between 1.5 ms and 7.5 ms (see table 1). For a given h_{rss} value, a higher σ in the time domain implies that the energy of the Gaussian is in the low-frequency region of the detection bandwidth, hence the detected *SNR* (and thus the detection efficiency) is lower. This causes the detection efficiency to decrease for increasing σ.

We compare our results for sine-Gaussian waveforms with Q=5, with those obtained by [9] for sine-Gaussian waveforms with $Q = 4.5$, in association with GRB 030329 during LIGO S2. The sensitivity of the Hanford detectors during S2 was similar to Virgo during C7. Moreover, the visibility of GRB 030329 from LIGO $\left(\sqrt{\left(F_+^0\right)^2 + \left(F_\times^0\right)^2} = 0.37\right)$ was nearly equal to the one of GRB 050915a from Virgo (0.38). LIGO's lowest strain upper limit, $h_{rss} = 2.1 \times 10^{-20}$ Hz$^{-1/2}$ (note that according to the different definitions, the upper limits reported in table I of [9] should be divided by $\sqrt{\frac{(F_+^0)^2+(F_\times^0)^2}{2}}$ before comparing with the results reported in our table 1, where the quoted h_{rss} strains do not contain the attenuation for the antenna pattern (see equation (5)), was obtained at $f_0 \sim 250$ Hz. In our case, we get the lowest value of $h_{rss} \sim 2.09 \times 10^{-20}$ Hz$^{-1/2}$ at $\sim$500 Hz. At higher frequencies, around 1000 Hz, the LIGO upper limit is $h_{rss} = 6.5 \times 10^{-20}$ Hz$^{-1/2}$, to be compared with $h_{rss} \sim 2.96 \times 10^{-20}$ Hz$^{-1/2}$ in the Virgo case. We stress that the LIGO procedure is based on the cross-correlation between the output of the two Hanford detectors, while our search is a single detector analysis.

6.4. *Astrophysical interpretation*

As described in section 5.5, GWs could give direct information on the GRB progenitor's identity. Of course, the critical aspect in theoretical models for the production of GWs in association with long GRBs is the fraction of energy expected to be emitted in GWs, E_{GW}, during the phases when dynamical instabilities develop.

Sources radiating energy E_{GW} could produce an extremely small $h(t)$ signal at the detector, depending on the emission pattern. Nevertheless, we can always associate a strain $h(t)$ at the detector with some minimum amount of E_{GW} radiated by the source, selecting an optimistic emission pattern. This is in fact the spirit of the analysis presented here, where attention was mostly devoted to those phases of GW emission dominated by a $l = m = 2$ emission pattern (i.e. having a maximum along the line of sight). If any GRB (at the sky location of GRB 050915a) happened at a distance of the order of $d_L = 40$ Mpc (where at least GRB 980425 is known to have occurred [78]), then the h_{rss} upper limit obtained for the sine-Gaussian waveform with $f_0 = 203$ Hz and $Q = 5$ would correspond to a radiated energy, E_{GW}, of (see

[36] or appendix B for details)

$$E_{GW} \simeq \left(h_{rss}^{SG}\right)^2 \frac{c^3 d_L^2 2\pi^2 f_0^2}{5G(1+z)} \tag{20}$$

which gives an energy upper limit of

$$E_{GW}^{UL} \simeq 350 M_\odot (d_L/40\,\mathrm{Mpc})^2. \tag{21}$$

When Virgo is running at its nominal sensitivity, the noise strain around ∼200 Hz is expected to be about a factor of 15 lower than during C7 (see figure 1). Thus, if we assume to have a *SNR* distribution confined below $SNR = 9$, then the energy upper limit given in equation (20) would be lowered by a factor of ∼225. Further improvement may also come in the case of optimal orientation: e.g. if GRB 050915a was optimally oriented with respect to the Virgo antenna pattern, the upper limit in equation (21) would be a factor of $\left(\left(F_+^0\right)^2 + \left(F_\times^0\right)^2\right)^{-1} \simeq 7$ lower. Moreover, the joint collaboration with LIGO will help in setting upper limits, since a coincidence search using three or four detectors will be a powerful tool in reducing the tail observed in the *SNR* distribution of the on-source region.

Some of the most optimistic predictions for the emission of GWs when instabilities develop in the rotating core of the massive GRB progenitor or in the disc surrounding the final BH, give an upper limit estimate of the order of $\sim 0.1 M_\odot$ (e.g. [45] for the case of a merger of two blobs of $1 M_\odot$ each, formed in the fragmentation of a collapsing core). We thus conclude that, *under the optimistic assumptions of optimal orientation and distance of 40 Mpc*, the Virgo detector at its nominal sensitivity will start reaching the level of theoretical upper limit estimates for GW emission by long GRB progenitors.

7. Conclusion

We have presented the first analysis of Virgo data in coincidence with a GRB trigger, aimed at searching for a burst of GWs associated with the long GRB 050915a, occurring during Virgo C7 run. We have analyzed a time window of 180 s around the GRB trigger time, and about 4.6 h of off-source data, corresponding to a single lock stretch. The result of this analysis is a set of loudest event upper limits on the strain of an astrophysical GW signal occurring in association with GRB 050915a. The evaluation of the pipeline and detector efficiency for detecting signals showing up as events with *SNR* above the loudest observed in the on-source region, was performed by adding a set of simulated burst-type signals to the off-source data, at randomly selected times. The waveforms of the simulated signals were chosen taking into account present uncertainties in the predictions for GW emission associated with GRB progenitors, linked with the ringing of the final BH.

The best upper limit strain amplitudes obtained in our analysis are of the order of $h_{rss} = (2–4) \times 10^{-20}\ \mathrm{Hz}^{-1/2}$ around ∼200–1500 Hz, affected by a ∼+20–40% systematic error. On the basis of these results we conclude that, when running at nominal sensitivity, Virgo will start putting interesting astrophysical constraints for GW emission in association with GRBs at distances comparable to GRB 980425.

Short GRBs, probably associated with the merger of compact binaries and occurring at lower redshifts [79, 80], will represent even more promising targets. The procedure for the analysis presented here may in fact also be extended to the study of these sources, especially for the phases of merger and ring-down, but also for the last stages of the earlier in-spiral phase. The kind of search implemented here, while expected to be less efficient than a matched filtering approach, has the great advantage of avoiding strong dependence on exact knowledge of the in-spiral waveforms. Finally, these kinds of studies will be of great benefit for the joint collaboration with LIGO, in view of which is the hope that a coincident detection could occur with three or four interferometers, during the explosion of a relatively near GRB.

Acknowledgments

The authors gratefully acknowledge the support of the Istituto Nazionale di Fisica Nucleare—INFN, of the Centre National de la Recherche Scientifique—CNRS, and of the European Gravitational Observatory—EGO. A Corsi acknowledges the support of a VESF fellowship, funded by EGO and hosted at Istituto di Astrofisica Spaziale e Fisica Cosmica—IASF-Rome/INAF, on the project titled 'Gravitational Waves by Gamma-Ray Bursts'. A Corsi also thanks Luigi Piro for useful comments/suggestions and Pietro Ubertini for hosting the VESF project at IASF-Rome.

Appendix A. Details on the sine-Gaussian waveform choice

In what follows, we review some results reported in the literature useful to address the question of how to mimic GW emission from collapse, fragmentation or bar instabilities, which is relevant for our GRB analysis.

Consider a source of GWs characterized by a mass quadrupole tensor $D_{i,j}$ [81] $(i, j = 1, 2, 3)$. The transverse–traceless components of the metric perturbation are related to the transverse–traceless components of the quadrupole tensor. In a system of orthonormal spherical coordinates (r, θ, ϕ), where the observer direction makes an angle θ_0 with the x_3-axis and ϕ_0 with the x_1-axis, the two non-vanishing components of the perturbation to the Galilean metric [81] read

$$h_\times = h_{\theta_0\phi_0} = -\frac{2G}{3c^4 d}\ddot{D}_{\theta_0\phi_0}, \tag{A.1}$$

$$h_+ = h_{\theta_0\theta_0} = -h_{\phi_0\phi_0} = -\frac{G}{3c^4 d}(\ddot{D}_{\theta_0\theta_0} - \ddot{D}_{\phi_0\phi_0}), \tag{A.2}$$

where $D_{\phi_0\phi_0}$, $D_{\theta_0\phi_0}$, $D_{\theta_0\theta_0}$ are the projections of the mass quadrupole tensor along the directions of the spherical unit vectors.

Consider now the particular case of a system characterized by a mass quadrupole tensor having $D_{31} = D_{13} = D_{32} = D_{23} = 0$, with respect to a set of fixed inertial axes (x_l, x_2, x_3), where the x_3-direction is the invariant one of the angular momentum or the rotation. A large class of realistic astrophysical systems, relevant also as GRB progenitors, turn out to have such a mass quadrupole tensor. These include e.g. binary systems, rotating ellipsoidal objects and pulsating/rotating ellipsoids [82]. For large amplitude pulsations, the latter case corresponds to explosion and collapse [83, 84]. Given the freedom of rotation about the x_3-axis (which, for a GRB, is the rotational axis along which the jet is launched), a reference system can always be chosen to have the observer on the x_1–x_3 plane ($\phi_0 = 0$). In the simplified assumption of a rigid, uniform, ellipsoid rotating with an angular velocity ω around the x_3-axis, $D_{i,j}$ has a time-independent expression $D'_{\alpha,\beta}$ in the frame x'_1, x'_2, x'_3 co-moving with the rigid rotating object, where non-diagonal elements are null (due to the reflection symmetry of the mass distribution). Expressing $D_{i,j}$ as a function $D'_{\alpha,\beta}$, one gets

$$h_\times = \frac{4G\omega^2}{3c^4 d}(D'_{11} - D'_{22})\sin(2\omega t)\cos\theta_0 \tag{A.3}$$

$$h_+ = \frac{1}{2}\frac{4G\omega^2}{3c^4 d}(D'_{11} - D'_{22})\cos(2\omega t)(1+\cos^2\theta_0). \tag{A.4}$$

For a GRB observed on-axis ($\theta_0 = 0$ in (A.3) and (A.4)), the signal is circularly polarized. Equations (A.3) and (A.4) do apply also to the case of a binary system or to a bar-like structure, which are all thought to play a role in GRB progenitors [46].

An equivalent but useful way to expand the waveforms is in terms of $l = 2$ pure-spin tensor harmonics. For a transverse–traceless tensor, in the quadrupole approximation, the only components that can enter are the basis states usually labeled as $T^{E2,lm}$ [85], so that $h_{ij}^{TT} = -\frac{2G}{c^4 d}\sum_m A_{2m}T^{E2,2m}$. Using the explicit representation of $T^{E2,lm}$ in orthonormal spherical coordinates (see [85] for details), one gets $A_{2\pm1} = 0 = A_{2\pm0}$ for a rigidly rotating ellipsoid. Thus, GW emission from rotating rigid ellipsoids or binary systems is dominated by the $l = |m| = 2$ mode, for which the wave amplitude is maximized along the rotational axis.

Appendix B. Energy radiated in GWs

In what follows we give details on the procedure followed to determine the energy upper limit for the sine-Gaussian waveform with $Q = 5$ at ~200 Hz.

The energy radiated in GWs is computed as

$$E_{GW} = \frac{c^3 d_L^2}{16\pi G}\int \mathrm{d}\Omega \int_{-\infty}^{+\infty} \left(\dot{h}_+^2(t) + \dot{h}_\times^2(t)\right)\frac{\mathrm{d}t}{1+z}, \tag{B.1}$$

where the integration over the solid angle should be performed while considering the emission pattern. If the signal power at the detectors is dominated by a frequency f_0, as is the case for the sine-Gaussian waveforms, the above formula is approximated as

$$E_{GW} \simeq \frac{c^3 d_L^2}{16\pi G}\left(4\pi^2 f_0^2\right)\int \mathrm{d}\Omega \int_{-\infty}^{+\infty} \left(h_+^2(t) + h_\times^2(t)\right)\frac{\mathrm{d}t}{1+z}. \tag{B.2}$$

On the basis of equations (A.3) and (A.4), we have

$$E_{GW} \simeq \frac{c^3 d_L^2 2\pi^2 f_0^2}{4G(1+z)}\int_{-1}^{1} d(\cos\theta)\int_{-\infty}^{+\infty} \mathrm{d}t \left[\frac{1}{4}(1+\cos^2\theta)^2 h_{+,0}^2(t) + \cos^2\theta\, h_{\times,0}^2(t)\right], \tag{B.3}$$

where $h_{+,0}(t)$ and $h_{\times,0}(t)$ are given by the plus and cross components in equations (10) and (11). Taking into account that $\int_{-\infty}^{+\infty} h_{\times,0}^2\,\mathrm{d}t = \int_{-\infty}^{+\infty} h_{+,0}^2\,\mathrm{d}t$, we can write

$$E_{GW} \simeq \frac{c^3 d_L^2 2\pi^2 f_0^2}{4G(1+z)}\int_{-1}^{1} d(\cos\theta)\left[\frac{1}{4}(1+\cos^2\theta)^2 + \cos^2\theta\right]\int_{-\infty}^{+\infty} \mathrm{d}t\, h_{+,0}^2(t). \tag{B.4}$$

The time integral is equal to $(h_{rss}^{SG})^2/2$, where h_{rss}^{SG} has the values quoted in table 1. Thus we write

$$E_{GW} \simeq (h_{rss}^{SG})^2 \frac{c^3 d_L^2 2\pi^2 f_0^2}{5G(1+z)}.$$

References

[1] Piran T 2005 *Rev. Mod. Phys.* **76** 1143
[2] Mészáros P 2006 *Rep. Prog. Phys.* **69** 2259
[3] Dezalay J-P *et al* 1992 *AIP Conf. Proc.* **265** 304
[4] Kouveliotou C *et al* 1993 *Astrophys. J.* **413** L101
[5] Mukherjee S *et al* 1998 *Astrophys. J.* **508** 314
[6] Preece R D *et al* 2000 *Astrophys. J. Suppl.* **126** 19
[7] www.virgo.infn.it
[8] Grupe D *et al* 2005 *GRB Coordinates Network* 3977

[9] Abbott B *et al* 2005 *Phys. Rev.* D **72** 042002
[10] Acernese F *et al* 2007 *Class. Quantum Grav.* **24** S381–8
[11] Rowan S and Hough J 2000 *Living Rev. Rel.* **3** 3 http://www.livingreviews.org/lrr-2000-3
[12] Maggiore M 2000 *Phys. Rep.* **331** 283
[13] Weinberg S 2004 *Phys. Rev.* D **69** 023503
[14] Lattanzi M and Montani G 2005 *Mod. Phys. Lett.* A **20** 2607
[15] Blanchet L 2006 *Living Rev. Rel.* **9** 4 http://www.livingreviews.org/lrr-2006-4
[16] Ferrari V *et al* 2004 *Mon. Not. R. Astron. Soc.* **350** 763
[17] Ferrari V *et al* 2004 *Class. Quantum Grav.* **21** 515
[18] Manca G M *et al* 2007 *Class. Quantum Grav.* **24** 171
[19] Fryer C L and New K C B 2003 *Living Rev. Rel.* **6** 2 http://www.livingreviews.org/lrr-2003-2
[20] Mohanty S D 2005 *Class. Quantum Grav.* **22** 1349
[21] Astone P *et al* 2005 *Phys. Rev.* D **71** 2001
[22] Màrka Sz and Mohanty S D 2005 *Nucl. Phys.* B **138** 446
[23] Mohanty S D *et al* 2004 *Class. Quantum Grav.* **21** S1831
[24] Astone P *et al* 2004 *Class. Quantum Grav.* **21** S759
[25] Cerdonio M *et al* 2004 *ASP Conf. Ser.* **312** 478
[26] Tricarico P, Ortolan A and Fortini P 2003 *Class. Quantum Grav.* **20** 3523
[27] Astone P *et al* 2002 *Phys. Rev.* D **66** 2002
[28] Modestino G and Moleti A 2002 *Phys. Rev.* D **65** 022005
[29] Tricarico P *et al* 2001 *Phys. Rev.* D **63** 2002
[30] Modestino G and Pizzella G 2000 *Astron. Astrophys.* **364** 419
[31] Murphy M T, Webb J K and Heng I K 2000 *Mon. Not. R. Astron. Soc.* **316** 657
[32] Finn L S, Mohanty S D and Romano J D 1999 *Phys. Rev.* D **60** 121101
[33] Amati L *et al* 1999 *Astron. Astrophys. Suppl. Ser.* **138** 605
[34] Astone P *et al* 1999 *Astron. Astrophys. Suppl. Ser.* **138** 603
[35] Abbott B *et al* 2007 *Preprint* arXiv:0711.1163
[36] Abbott B *et al* 2008 *Phys. Rev.* D **77** 062004
[37] Acernese F *et al* 2006 *Class. Quantum Grav.* **23** S635
[38] Beauville F 2005 Prélude à l'analyse des donnees du detecteur Virgo: de l'étalonnage à la recherche de coalescences binaires *PhD Thesis*
[39] http://www.ligo.caltech.edu/~jzweizig/distribution/LSC_Data
[40] Woosley S E 1993 *Astrophys. J.* **405** 273
[41] Paczyńsky B 1998 *Astrophys. J.* **494** L45
[42] Fryer C, Woosley S E and Hartmann D H 1999 *Astrophys. J.* **526** 152
[43] Frail D A *et al* 2001 *Astrophys. J.* **562** L55
[44] Mészáros P 1999 *Prog. Theor. Phys. Suppl.* **136** 300
[45] Kobayashi S and Mészáros P 2003 *Astrophys. J.* **589** 861
[46] Kobayashi S and Mészáros P 2003 *Astrophys. J.* **585** L89
[47] Zhang B and Mészáros P 2004 *Int. J. Mod. Phys.* A **19** 2385
[48] Putten M H *et al* 2004 *Phys. Rev.* D **69** 044007
[49] Gehrels N *et al* 2004 *Astrophys. J.* **611** 1005
[50] Barthelmy S *et al* 2005 *GRB Coordinates Network* 3982
[51] Grupe D *et al* 2005 *GRB Coordinates Network* 3983
[52] Blustin J A *et al* 2005 *GRB Coordinates Network* 3986
[53] Yost S A *et al* 2005 *GRB Coordinates Network* 3978
[54] Kilmartin P and Gilmore A 2005 *GRB Coordinates Network* 3980
[55] Cenko S B and Fox D B 2005 *GRB Coordinates Network* 3981
[56] Weidong L 2005 *GRB Coordinates Network* 3985
[57] Bloom J S and Alatalo K 2005 *GRB Coordinates Network* 3984
[58] Bloom J S 2005 *GRB Coordinates Network* 3990
[59] Cameron P B and Frail D A 2005 *GRB Coordinates Network* 4001
[60] Jakobsson P *et al* 2007 *Proc. 11th Marcel Grossmann Meeting on General Relativity* ed H Kleinert, R T Jantzen and R Ruffini (Singapore: World Scientific) (*Preprint* astro-ph/0611561)
[61] Ovaldsen J-E *et al* 2007 *Astrophys. J.* **662** 294
[62] Daubechies I 1992 *Ten Lectures on Wavelets (CBMS-NSF Reg. Conf. Series in Applied Math.)* (Philadelphia, PA: SIAM)
[63] Dohono D and Johnston I 1992 *Biometrika* **81** 425

[64] Mallat S 1999 *A Wavelet Tour of Signal Processing* (New York: Academic)
[65] http://gcn.gsfc.nasa.gov/swift2005_grbs.html
[66] Cuoco E 2005 *'Wavelet de-noising strategy for transient waveforms identification',* VIR-NOT-EGO-1390-305
[67] Caron B *et al* 1999 *Appl. Phys.* **10** 369
[68] Thorne K S 1987 Gravitational radiation *300 Years of Gravitation* ed S W Hawking and W Israel (Cambridge: Cambridge University Press)
[69] Finn L S and Chernoff D F 1993 *Phys. Rev.* D **47** 2198
[70] Klimenko S *et al* 2005 *Phys. Rev. D.* **72** 122002
[71] Fryer C L, Holz S A and Hughes S A 2002 *Astrophys. J.* **565** 430
[72] Berti E, Cardoso V and Will C M 2006 *Phys. Rev.* D **73** 4030
[73] Ferrari V, Gualtieri L and Rezzolla L 2006 *Phys. Rev.* D **73** l24028
[74] Rhook K J and Wyithe J S B 2005 *Mon. Not. R. Astron. Soc.* **361** 1145
[75] Echeverria F 1989 *Phys. Rev.* D **40** 3194
[76] Acernese F *et al* 2007 *Class. Quantum Grav.,* at press
[77] Brady P R, Creighton J D E and Wiseman A G 2004 *Class. Quantum Grav.* **21** S1775
[78] Pian E *et al* 1999 *Astron. Astrophys. Suppl. Ser.* **138** 463
[79] Berger E 2006 *Proc. 16th Annual October Astrophysics Conf. in Maryland Gamma Ray Bursts in the Swift Era* ed S Holt, N Gehrels and J Nousek (*Preprint* astro-ph/0602004)
[80] Nakar E 2007 *Phys. Rep.* **442** 166
[81] Landau L and Lifshitz E 1975 *The Classical Theory of Fields* (London: Pergamon)
[82] Beltrami H and Chau W Y 1985 *Astrophys. Space Sci.* **111** 335
[83] Beltrami H and Chau W Y 1986 *Astrophys. Space Sci.* **119** 353
[84] Saenz R A and Shapiro S L 1978 *Astrophys. J.* **221** 286
[85] Kochanek C S *et al* 1990 *Astrophys. J.* **358** 81